IET Microwaves, Antennas & Propagation

The Institution of Engineering and Technology **WILEY**

ORIGINAL RESEARCH PAPER

Radiation characteristics of a double-layer spherical dielectric lens antenna with a conformal PEC disk fed by on-axis dipoles

Maria E. Tikhenko[1] | Valery V. Radchenko[2] | Sergii V. Dukhopelnykov[1,3] | Alexander I. Nosich[3]

[1]Department of Applied Mathematics, V. N. Karazin Kharkiv National University, Kharkiv, Ukraine

[2]Department of Mathematics, Kharkiv National Academy of Municipal Economy, Kharkiv, Ukraine

[3]Laboratory of Micro and Nano Optics, Institute of Radio-Physics and Electronics NASU, Kharkiv, Ukraine

Correspondence

Alexander I. Nosich, O.Ya. Usikov Institute for Radiophysics and Electronics, NASU, 12, Ac. Proskura St, Kharkov 61085, Ukraine.
Email: anosich@yahoo.com

Funding information

National Research Foundation of Ukraine, Grant/Award Number: 2020.02.0150

Abstract

The radiation of a double-layer spherical dielectric lens equipped with a conformal spherical-disk PEC reflector and excited by elementary sources located on the antenna axis of rotation is considered. The sources are either a radial electric dipole or a tangential magnetic dipole. Using the analytical inversion of the static part of the homogeneous-lens problem with the aid of the Abel integral transform, developed earlier for plane-wave scattering, each of the considered problems are cast to the Fredholm second-kind infinite matrix equation with elements containing only the elementary functions. This guarantees convergence and enables accurate characterisation of the considered lens antennas in terms of directivity and total radiated power, in wide frequency range. It is demonstrated that the best directivity is provided by the quasi-Luneburg lens configuration with dielectric constants of the core and the shell being 2 and 1.1, respectively, shell thickness being 0.1 of the outer lens radius, and reflector size around 30°. This performance, however, is spoiled by the whispering-gallery-mode resonances that can be effectively alleviated by the introduction of the moderate losses to the shell material.

1 | INTRODUCTION

Homogeneous dielectric sphere is the simplest lens with the focal point emerging off the lens, according to the geometrical optics (GO), if its dielectric constant is less than 4 [1]. A non-homogeneous Luneburg lens was proposed in [2] on the basis of GO analysis of the focussing by a dielectric sphere with dielectric constant equal to two in the centre and 1 at the boundary; GO predicts the focal point just on its surface. Its more practical version, a discrete Luneburg lens fed by a small horn was apparently introduced to microwave antenna technology [3–7]. The interest in spherical-lens antennas soon faded off because of the absence of low-loss dielectric materials and strong competition from other antennas. In the 1990s, however, this interest emerged again with an emphasis on millimetre-wave point-to-multipoint communication [8], and since then most of the technological problems seem to have been overcome. New application areas have appeared,

such as radio astronomy and vehicle radar [9, 10]. In terms of the spherical lens theory and modelling, the shape of such a lens offers the rare opportunity to solve analytically the wave scattering problems by reducing them to the Mie series. However, any dielectric antenna consists of not only a lens but also a feed, which is frequently a small horn or a printed circuit. Therefore, the following steps are important: solving the discrete Luneburg lens fed by a Huygens source (crossed elementary electric and magnetic dipoles) [11] and by a complex-source-point (CSP) as a model of beam radiated by an aperture and having controlled beam-width [12]. Apart from that, since the early 1990s there has appeared new interest in even shorter waves of the terahertz and sub-millimetre ranges. Here, of course, quasi-optical approaches are even more appropriate; hence, it is no surprise that dielectric lenses are the key components of all terahertz systems. It was in this context that the concept of the integrated lens antenna (ILA) appeared.

The ILA combines an essentially quasi-optical principle (focussing) with a resonance effect (in the printed cavity); in terms of engineering, it has turned out to be quite successful. However, it introduced a huge challenge to the accurate simulation efforts because the theories put in the core of the modelling of these two components (lens and printed circuit) are drastically different.

On the one hand, GO and other high-frequency asymptotic approaches usually applied to the lenses' analyses fail completely to reproduce the field features associated with wavelength-size printed components. On the other hand, no conventional MoM code can avoid failure if applied to a printed feed plus a 30-wavelength diameter dielectric-lens problem. Generally speaking, any ILA should a priori display a complicated interplay of both ray-like and mode-like phenomena. This circumstance calls for the use of full-wave techniques; however, so economic and fast that even the quasi-optical effects arising when the lens has a few dozen wavelength size, can be addressed accurately and in reasonable time.

As is well-known, such high performance can be achieved either with the method of analytical regularisation (MAR) [13] or with the Nystrom-type discretisations applied to the integral equations [14]. In particular, the MAR based on the analytical regularisation of the dual-series equations was developed in [15–18] for the analysis of several spherical antennas and scatterers, equipped with a perfectly electrically conducting (PEC) spherical disk, however, only under the normal incidence. The double PEC disk circuit, integrated with a discrete Luneburg lens and fed by a radial Hertz electric dipole (RED) and a tangential Hertz magnetic dipole (TMD) was analysed with the same scheme in [19]. The arbitrary plane-wave incidence was successfully handled by the MAR on regularising the Galerkin projection [20, 21] for the discrete Luneburg lens and homogeneous spherical lens, equipped with a conformal PEC spherical-disk reflector.

The aim of our work is to check how the directivity of a dipole-fed homogeneous spherical lens antenna can be further improved by combined use of a PEC disk reflector and an additional thin shell layer. In our study, we will follow [15–19] because on-axis dipoles enforce either no or simple azimuth dependence. An additional merit is that this approach leads to the Fredholm second-kind matrix equations that do not involve numerical integrations for filling in the matrix.

2 | MATHEMATICAL FORMULATION AND BASIC EQUATIONS

Here we consider a double-layer spherical, dielectric lens antenna excited by an on-axis RED or TMD and backed with a conformal spherical PEC reflector (Figure 1). The non-magnetic lens core and shell have relative dielectric constants of ε_1 and ε_2, respectively. The zero-thickness reflector has an angular width of $2\theta_0$ in the spherical coordinates (r, φ, θ). The RED or TMD source is located in the shell layer.
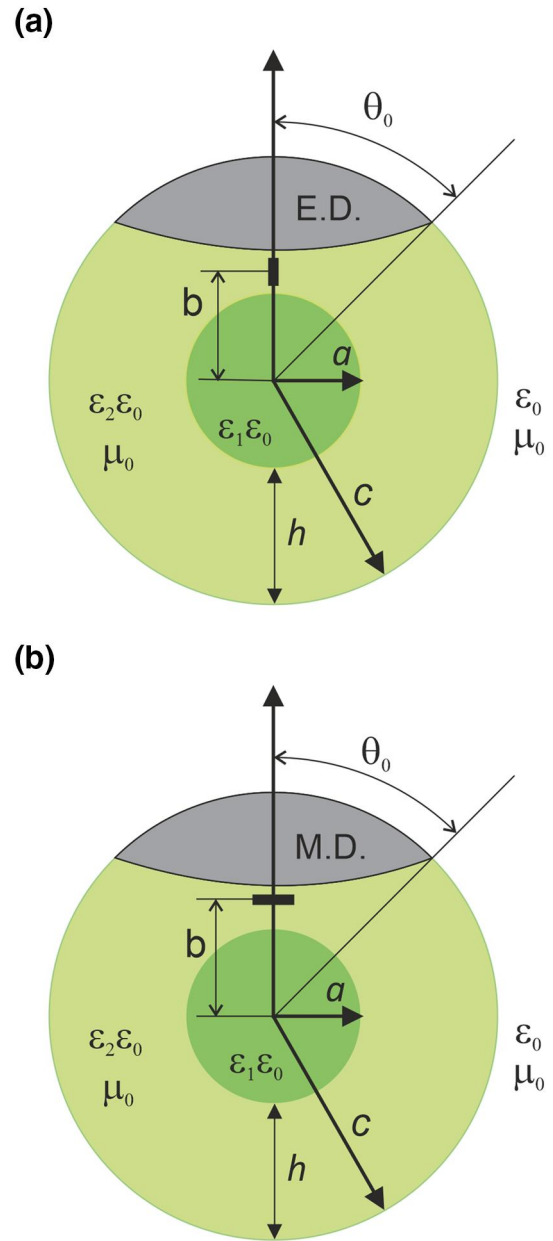

FIGURE 1 Core-shell spherical dielectric lens with conformal perfectly electrically conducting disk fed by radial electric (a) and tangential magnetic (b) dipoles

2.1 | Lens excitation with on-axis RED

The considered electromagnetic field problem is three-dimensional but rotationally symmetric. The total field in the presence of the lens must satisfy the Maxwell equations, the boundary and continuity conditions for the tangential field components on the PEC reflector and material interfaces, respectively, the edge condition (local power finiteness), and the Silver-Muller outgoing radiation condition at infinity.

We introduce three partial domains: "#1" is the lens core, "#2" is the lens shell, and "3" is the space outside the lens. The dipole source, RED, is assumed to be in domain "#2".

Following [17] and using the addition theorem for the spherical harmonics, we present the field components of the RED tangential to the lens surface as the following expansions:

$$E_\theta^{(0)} = \frac{Z_0 B}{\sqrt{\varepsilon}} \sum_{n=1}^\infty (2n+1) \begin{Bmatrix} \psi_n(kb)\zeta'_n(kr), & r>b \\ \zeta_n(kb)\psi'_n(kr), & r<b \end{Bmatrix} P_n^1(\cos\theta), \quad (1)$$

$$H_\varphi^{(0)} = B \sum_{n=1}^\infty (2n+1) \begin{Bmatrix} \psi_n(kb)\zeta_n(kr), & r>b \\ \zeta_n(kb)\psi_n(kr), & r<b \end{Bmatrix} P_n^1(\cos\theta) \quad (2)$$

where $E_\varphi^{(0)} = 0$, $H_\theta^{(0)} = 0$. Here, the RED is assumed to be shifted by the distance b along the symmetry axis in the medium with the relative dielectric constant ε. Besides, the following notations are introduced: $\psi_n(\cdot)$ and $\zeta_n(\cdot)$ are the spherical Bessel and Hankel (first-kind) functions, respectively, in the Debye notations, $P_n^1(\cdot)$ are the associated Legendre functions of the first kind, $k_0 = \omega/c$, $k = k_0\sqrt{\varepsilon}$, $Z_0 = \sqrt{\mu_0/\varepsilon_0}$ is the free-space impedance, and $p = I_0^e l$, where I_0^e is the amplitude of the electric current in the dipole and l is the length of dipole, $B = -p(4\pi kb^2 r)^{-1}$.

Taking into account (1) and (2), we look for the total field components in each space domain in terms of similar series with unknown coefficients. In the domain "#1" ($r < a$),

$$E_\theta^{(1)} = \frac{Z_0 B}{\sqrt{\varepsilon_1}} \sum_{n=1}^\infty (2n+1) t_n \psi'_n(k_1 r) P_n^1(\cos\theta), \quad (3)$$

$$H_\varphi^{(1)} = \sum_{n=1}^\infty (2n+1) t_n \psi_n(k_1 r) P_n^1(\cos\theta), \quad (4)$$

In the domain "#2" ($a < r < c$), $E^{(2)} = E^{(0)} + E^{(2)sc}$, $H^{(2)} = H^{(0)} + H^{(2)sc}$, where $E^{(0)}$, $H^{(0)}$ stand for the dipole field components from (1) and (2), and $E^{(2)sc}$, $H^{(2)sc}$ are for the components of the scattered field.

$$E_\theta^{(2)sc} = \frac{Z_0 B}{\sqrt{\varepsilon_2}} \sum_{n=1}^\infty (2n+1) \left[x_n \psi'_n(k_2 r) + y_n \zeta'_n(k_2 r) \right] P_n^1(\cos\theta), \quad (5)$$

$$H_\varphi^{(2)sc} = B \sum_{n=1}^\infty (2n+1) \left[x_n \psi_n(k_2 r) + y_n \zeta_n(k_2 r) \right] P_n^1(\cos\theta), \quad (6)$$

In the domain "#3" ($r > c$),

$$E_\theta^{(3)} = Z_0 B \sum_{n=1}^\infty (2n+1) z_n \zeta'_n(k_0 r) P_n^1(\cos\theta), \quad (7)$$

$$H_\varphi^{(3)} = B \sum_{n=1}^\infty (2n+1) z_n \zeta_n(k_0 r) P_n^1(\cos\theta) \quad (8)$$

Note that the above expansions already satisfy the Maxwell equations and the outgoing radiation condition, in term-by-term manner. Hence, now we have to find the unknown coefficients $\{t_n, x_n, y_n, z_n\}_{n=1}^\infty$ using the boundary conditions and the edge condition at the reflector's rim.

The conditions at the lens' core-shell boundary are the continuity conditions of the field tangential components.

$$E_\theta^{(1)}|_{r=a} = E_\theta^{(2)}|_{r=a}, \quad H_\varphi^{(1)}|_{r=a} = H_\varphi^{(2)}|_{r=a}, \quad (9)$$

The conditions at the outer surface of the lens shell are of the mixed type: they are the continuity conditions of the tangential components at the dielectric surface and the vanishing of the electric field at the PEC reflector.

$$E_\theta^{(2)}|_{r=c} = E_\theta^{(3)}|_{r=c} = 0, \quad \text{if } \theta \in [0, \theta_0) \quad (10\text{-}a)$$

$$H_\varphi^{(2)}|_{r=c} = H_\varphi^{(3)}|_{r=c}, \quad \text{if } \theta \in (\theta_0, \pi] \quad (10\text{-}b)$$

Further, we eliminate some of the unknown coefficients so that only one of the four sets remains. Then the mixed conditions (10) lead to the following dual-series equation (DSE):

$$\begin{cases} \sum_{n=1}^\infty \tilde{z}_n (1 - \Delta_n) P_n^1(\cos\theta) = 0, & \theta \in [0, \theta_0), \\ \sum_{n=1}^\infty \frac{(2n+1)}{n(n+1)} \tilde{z}_n P_n^1(\cos\theta) = \sum_{n=1}^\infty (2n+1) \alpha_n P_n^1(\cos\theta), & \theta \in (\theta_0, \pi], \end{cases} \quad (11)$$

where

$$\Delta_n = 1 + \frac{(1+\varepsilon_2)}{2} k_0 c \frac{(2n+1)}{n(n+1)}$$
$$\times \left\{ \frac{\zeta_n(k_0 c)}{\zeta'_n(k_0 c)} - \frac{\sqrt{\varepsilon_2}\zeta'_n(k_0 c)[A_n\psi_n(k_2 c) + B_n\zeta_n(k_2 c)]}{A_n\psi'_n(k_2 c) + B_n\zeta'_n(k_2 c)} \right\}^{-1} \quad (12)$$

$$\alpha_n = \frac{1}{\sqrt{\varepsilon_2}} \left\{ \frac{\psi_n(k_2 b)\zeta'_n(k_2 c) - \zeta_n(k_2 b)\psi'_n(k_2 c)}{A_n\psi'_n(k_2 c) + B_n\zeta'_n(k_2 c)} \right.$$
$$\left. \times [A_n\psi_n(k_2 c) + B_n\zeta_n(k_2 c)] + \zeta_n(k_2 b)\psi_n(k_2 c) - \psi_n(k_2 b)\zeta_n(k_2 c) \right\} \quad (13)$$

$$z_n = \frac{\tilde{z}_n}{n(n+1)} \left\{ \frac{\sqrt{\varepsilon_2}\zeta'_n(k_0 c)[A_n\psi_n(k_2 c) + B_n\zeta_n(k_2 c)]}{A_n\psi'_n(k_2 c) + B_n\zeta'_n(k_2 c)} - \zeta_n(k_0 c) \right\}^{-1} \quad (14)$$

$$A_n = \psi_n(k_1 a)\zeta'_n(k_2 a) - \psi'_n(k_1 a)\zeta_n(k_2 a)\sqrt{\varepsilon_2/\varepsilon_1}, \quad (15)$$

$$B_n = \psi_n(k_2 a)\psi'_n(k_1 a)\sqrt{\varepsilon_2/\varepsilon_1} - \psi'_n(k_2 a)\psi_n(k_1 a), \quad (16)$$

$$t_n = i\sqrt{\frac{\varepsilon_1}{\varepsilon_2}} \frac{[z_n\zeta'_n(k_0 c)\varepsilon_2 + \zeta_n(k_2 b)\psi'_n(k_2 c) - \psi_n(k_2 b)\zeta'_n(k_2 c)]}{A_n\psi'_n(k_2 c) + B_n\zeta'_n(k_2 c)}$$
$$(17)$$

$$x_n = -\zeta_n(k_2 b) - i\sqrt{\varepsilon_2/\varepsilon_1}\, t_n A_n \quad (18)$$

Now we can integrate the first of Equation (11) in θ and take into account that $\int P_n^1(\cos\theta)d\theta = C - P_n(\cos\theta)$, where C is an arbitrary constant. Then we obtain,

$$\sum_{n=1}^{\infty} \tilde{z}_n(1-\Delta_n)P_n(\cos\theta) = CP_0(\cos\theta), \quad \theta \in [0,\theta_0), \quad (19)$$

The derived DSE can be further transformed with the aid of the Abel integral transform, applied term-by-term to the Legendre polynomials and associated functions.

$$P_n(\cos\theta) = \frac{\sqrt{2}}{\pi} \int_0^\theta \frac{\cos[(n+1/2)\vartheta]d\vartheta}{\sqrt{\cos\vartheta - \cos\theta}}, \quad (20)$$

$$P_n^1(\cos\theta) = \frac{-2\sqrt{2}}{\pi\sin\theta} \frac{n(n+1)}{2n+1} \int_\theta^\pi \frac{\cos[(n+1/2)\theta]\sin\vartheta d\vartheta}{\sqrt{\cos\theta - \cos\vartheta}} \quad (21)$$

As the homogeneous Abel integral equation has only zero solution, the integrand functions in the transformed equations must vanish. Hence, we obtain a new DSE in terms of the trigonometric functions.

$$\begin{cases} \sum_{n=1}^{\infty} \tilde{z}_n(1-\Delta_n)\cos\left(n+\frac{1}{2}\right)\theta = C\cos(\theta/2), & \theta \in [0,\theta_0), \\ \sum_{n=1}^{\infty} \tilde{z}_n \cos\left(n+\frac{1}{2}\right)\theta = \sum_{n=1}^{\infty} n(n+1)\alpha_n\cos\left(n+\frac{1}{2}\right)\theta, & \theta \in (\theta_0,\pi], \end{cases}$$
$$(22)$$

Note that $\Delta_n = O(k_0^2 c^2 n^{-1}) + O((a/c)^{2n+1}) \to 0$ if $k_0 c \to 0$ or $n \to \infty$. Thus, the main part of this DSE corresponds to the static problem for a homogeneous sphere with a PEC cap. It can be analytically inverted using the inverse Fourier transform [17, 18]. After the exclusion of the constant C, the following infinite-matrix equation is obtained for $\tilde{z}_n$:

$$\tilde{z}_m - \sum_{n=1}^{\infty} \tilde{z}_m\Delta_n Q_{nm}^{(1)}(\theta_0) = \sum_{n=1}^{\infty} n(n+1)\alpha_n[\delta_n^m - Q_{nm}^{(1)}(\theta_0)],$$
$$(23)$$

where

$$Q_{nm}^{(1)}(\theta_0) = Q_{nm}(\theta_0) - Q_{0m}(\theta_0)Q_{n0}(\theta_0)Q_{00}^{-1}(\theta_0), \quad (24)$$

$$Q_{nm}(\theta_0) = \frac{\sin(m-n)\theta_0}{\pi(m-n)} + \frac{\sin(m+n+1)\theta_0}{\pi(m+n+1)} \quad (25)$$

Since $\sum_{m,n=0}^{\infty}|\Delta_n Q_{nm}^{(1)}|^2 < \infty$, (23) is a Fredholm operator equation of the second kind in the space of numerical sequences l_2 ($\tilde{z} \in l_2$ if $\sum_{n=0}^{\infty}|\tilde{z}_n|^2 < \infty$) under the condition that the right hand part vector also belongs to l_2, that holds true provided that $a < b < c$. Then, the Fredholm alternative guarantees the solution's existence in l_2, as the uniqueness of the solution is provided by the equivalence to the boundary-value problem for Maxwell equations. Moreover, after the truncation of (23) to a finite order N, the convergence at $N \to \infty$, by the l_2-norm, is guaranteed [13].

In the RED-excited antenna modelling, we are interested in the radiation resistance defined as

$$R = 2\bar{P}/|I_0^e|^2, \quad (26)$$

where the power radiated by the antenna is

$$\bar{P} = \frac{Z_0}{8\pi} \frac{(k_0 p)^2}{(k_0 b)^4} \sum_{n=1}^{\infty} n(n+1)(2n+1)|z_n|^2 \quad (27)$$

This value is conveniently normalised by the radiation resistance associated with a dipole in the free space.

$$R_0 = (6\pi)^{-1}Z_0 k_0^2 p^2/|I_0^e|^2 \quad (28)$$

Note that if $I_0^e = const$ then $R/R_0 = \bar{P}/P_0$.
The directivity of the antenna is defined as

$$D = 4\pi r^2 P_{max}/\bar{P}, \quad (29)$$

where P_{max} is the power radiated in the main beam direction that entails

$$D = \frac{Z_0}{4\pi\bar{P}} \frac{(k_0 p)^2}{(k_0 b)^4}\left|\sum_{n=1}^{\infty}(-i)^n(2n+1)z_n P_n^1(\cos\theta_{max})\right|^2 \quad (30)$$

Note that for an RED in the free space the directivity is $D_0 = 3/2$ and the main-beam direction is $\theta_{max} = 90^o$.

2.2 | Lens excitation with on-axis TMD

Unlike the previous case, this problem is not rotationally symmetric; hence, all six components of the field are present. Still, they have only one variation in azimuth, expressed by either $\sin\varphi$ or $\cos\varphi$ function.

The field components of the TMD shifted by the distance b along the symmetry axis in the medium with dielectric constant ε can be expanded in terms of the spherical harmonics similarly to the RED case (1) and (2). For instance,

$$
E_\theta^{(0)} = \frac{iq\sin\varphi}{4\pi br} \sum_{n=1}^{\infty} \frac{(2n+1)}{n(n+1)} \left[\sum_{n=1}^{\infty} \left\{ \begin{array}{l} \psi_n(k_2 b)\zeta_n'(kr), \ \ r>b \\ \\ \zeta_n(k_2 b)\psi_n'(kr), \ \ r<b \end{array} \right\} \right.
$$
$$
\left. \times \frac{\partial P_n^1(\cos\theta)}{\partial\theta} + \left\{ \begin{array}{l} \psi_n'(k_2 b)\zeta_n(kr), \ \ r>b \\ \\ \zeta_n'(k_2 b)\psi_n(kr), \ \ r<b \end{array} \right\} \frac{P_n^1(\cos\theta)}{\sin\theta} \right]
\tag{31}
$$

Other components have similar expansions.

Here $q = I_0^m l$, where I_0^m is the amplitude of the magnetic current in the dipole and l is the length of the dipole.

Taking into account (31), we expand the total field components in each space domain in the similar series with unknown coefficients.

Namely, in the domain "1" ($r < a$),

$$
E_\theta^{(1)} = \frac{iq\sin\varphi}{4\pi br} \sum_{n=1}^{\infty} \frac{(2n+1)}{n(n+1)} \left[t_n^{(e)}\psi'_n(k_1 r) \frac{\partial P_n^1(\cos\theta)}{\partial\theta} \right.
$$
$$
\left. + t_n^{(m)}\psi_n(k_1 r) \frac{P_n^1(\cos\theta)}{\sin\theta} \right],
\tag{32}
$$

in the domain "2" ($a < r < c$),

$$
E_\theta^{(2)sc} = \frac{iq\sin\varphi}{4\pi br} \sum_{n=1}^{\infty} \frac{(2n+1)}{n(n+1)} \left[\left\{ x_n^{(e)}\psi_n'(k_2 r) + y_n^{(e)}\zeta_n'(k_2 r) \right\} \right.
$$
$$
\left. \times \frac{\partial P_n^1(\cos\theta)}{\partial\theta} + \left\{ x_n^{(m)}\psi_n(k_2 r) + y_n^{(m)}\zeta_n(k_2 r) \right\} \frac{P_n^1(\cos\theta)}{\sin\theta} \right],
\tag{33}
$$

and in the domain "3" ($r > c$),

$$
E_\theta^{(3)} = \frac{iq\sin\varphi}{4\pi br} \sum_{n=1}^{\infty} \frac{(2n+1)}{n(n+1)} \left[z_n^{(e)}\zeta_n'(k_0 r) \frac{\partial P_n^1(\cos\theta)}{\partial\theta} \right.
$$
$$
\left. + z_n^{(m)}\zeta_n(k_0 r) \frac{P_n^1(\cos\theta)}{\sin\theta} \right]
\tag{34}
$$

Then, on introducing the notations

$$
f(\theta) = \sum_{n=1}^{\infty} \frac{(2n+1)}{n(n+1)} z_n^{(e)}\zeta_n'(k_0 c) P_n^1(\cos\theta),
\tag{35}
$$

$$
g(\theta) = -\sum_{n=1}^{\infty} \frac{(2n+1)}{n(n+1)} z_n^{(m)}\zeta_n(k_0 c) P_n^1(\cos\theta)
\tag{36}
$$

and using the boundary conditions valid on the interval $\theta \in [0, \theta_0)$, we obtain the following set of two coupled ordinary differential equations:

$$
\frac{1}{\sin\theta}f(\theta) - \frac{d}{d\theta}g(\theta) = 0,
\tag{37-a}
$$

$$
\frac{d}{d\theta}f(\theta) - \frac{1}{\sin\theta}g(\theta) = 0
\tag{37-b}
$$

It is easy to see that

$$
\frac{d}{d\theta}\left[\sin\theta \frac{d}{d\theta}f(\theta) \right] - \frac{1}{\sin\theta}f(\theta) = 0,
\tag{38-a}
$$

$$
g(\theta) = \sin\theta \frac{d}{d\theta}f(\theta), \ \ \theta \in [0, \theta_0)
\tag{38-b}
$$

The general solution of Equation (38-a) for $f(\theta)$ has the following form:

$$
f(\theta) = A_1 \tan(\theta/2) + A_2 \cot(\theta/2)
\tag{39}
$$

However, as $\cot(\theta/2) \to \infty$ if $\theta \to 0$, which contradicts the demand of the solution finiteness, we conclude that $A_2 \equiv 0$; thus, $f(\theta) = A_1 \tan(\theta/2)$ and the index in A can be dropped. Therefore, finally we find that

$$
f(\theta) = g(\theta) = A \tan(\theta/2), \ \ \theta \in [0, \theta_0)
\tag{40}
$$

Coming back to the series representations of the functions $f(\theta)$ and $g(\theta)$, we obtain the equations valid at $\theta \in [0, \theta_0)$,

$$
\sum_{n=1}^{\infty} \frac{(2n+1)}{n(n+1)} z_n^{(e)}\zeta_n'(k_0 c) P_n^1(\cos\theta) = A \tan(\theta/2),
\tag{41-a}
$$

$$
-\sum_{n=1}^{\infty} \frac{(2n+1)}{n(n+1)} z_n^{(m)}\zeta_n(k_0 c) P_n^1(\cos\theta) = A \tan(\theta/2),
\tag{41-b}
$$

The series equations valid at the interval of $\theta \in (\theta_0, \pi]$ that completes the spherical segment $\theta \in [0, \theta_0)$ to the full sphere of the radius $r = c$ can be derived in similar manner by using the corresponding boundary conditions and observing that the functions analogous to (40) in this case should be finite if $\theta \to \pi$. On introducing the notations

$$d_n = \psi_n(k_2 b)\zeta_n(k_2 c), \quad d'_n = \psi'_n(k_2 b)\zeta'_n(k_2 c), \qquad (42)$$

we obtain

After algebraic manipulations aimed at bringing together equations with 'electrical' $\{x_n^{(e)}, y_n^{(e)}, z_n^{(e)}\}$ and 'magnetic' coefficients, $\{x_n^{(m)}, y_n^{(m)}, z_n^{(m)}\}$, and exclusion of some of them using the continuity of the tangential electric field components across the whole spherical surface $r = c$, we obtain two coupled DSEs (44) and (45) in terms of the associated Legendre functions of the first kind, for each of two sets of 'electric' and 'magnetic' unknowns.

Here, we have also denoted

$$\tilde{z}_n^{(e)} = (2n+1)\zeta_n(k_0 c)z_n^{(e)}, \qquad (46)$$

$$-\sum_{n=1}^{\infty} \frac{(2n+1)}{n(n+1)} \left\{ z_n^{(e)}\zeta_n(k_0 c) - \sqrt{\varepsilon_2} \left[x_n^{(e)}\psi_n(k_2 c) + y_n^{(e)}\zeta_n(k_2 c) + d_n \right] \right\} P_n^1(\cos\theta) = B\cot(\theta/2), \;\; \theta \in (\theta_0, \pi],$$

$$(43)$$

$$\sum_{n=1}^{\infty} \frac{(2n+1)}{n(n+1)} \left\{ z_n^{(m)}\zeta'_n(k_0 c) - \sqrt{\varepsilon_2} \left[x_n^{(m)}\psi'_n(k_2 c) + y_n^{(m)}\zeta'_n(k_2 c) + d'_n \right] \right\} P_n^1(\cos\theta) = B\cot(\theta/2), \;\; \theta \in (\theta_0, \pi]$$

$$\begin{cases} \displaystyle\sum_{n=1}^{\infty} \frac{(2n+1)}{n(n+1)} \left(1 - \Delta_n^{(e)} \right)\tilde{z}_n^{(e)} P_n^1(\cos\theta) = -A2k_0 c\tan(\theta/2), \theta \in [0, \theta_0) \\[4mm] \displaystyle\sum_{n=1}^{\infty} \frac{(2n+1)}{n(n+1)} \left[-\alpha_n^{(e)} + \tilde{z}_n^{(e)} \right] P_n^1(\cos\theta) = -B\cot(\theta/2), \quad \theta \in (\theta_0, \pi] \end{cases} \qquad (44)$$

$$\begin{cases} \displaystyle\sum_{n=1}^{\infty} \frac{1}{n(n+1)} \left(1 - \Delta_n^{(m)} \right)\tilde{z}_n^{(m)} P_n^1(\cos\theta) = \frac{-A}{2k_0 c}\tan(\theta/2), \;\; \theta \in [0, \theta_0) \\[4mm] \displaystyle\sum_{n=1}^{\infty} \frac{(2n+1)}{n(n+1)} \left[-\alpha_n^{(m)} + \tilde{z}_n^{(m)} \right] P_n^1(\cos\theta) = -B\cot(\theta/2), \theta \in (\theta_0, \pi] \end{cases} \qquad (45)$$

$$\tilde{z}_n^{(m)} = -\zeta'_n(k_0c)z_n^{(m)} \tag{47}$$

$$\Delta_n^{(e)} = 1 + \frac{2(k_0c)\zeta'_n(k_0c)}{(2n+1)\zeta_n(k_0c)}, \tag{48}$$

$$\Delta_n^{(m)} = 1 + \frac{(2n+1)\zeta_n(k_0c)}{2(k_0c)\zeta'_n(k_0c)}, \tag{49}$$

$$\frac{\alpha_n^{(e)}}{(2n+1)} = -\left\{ \frac{\zeta'_n(k_0c)}{\zeta_n(k_0c)} - \frac{\Lambda^{(e)}}{\sqrt{\varepsilon_2}} \right\}^{-1} \Big[(d_n - \psi_n(k_2c)\zeta_n(k_2b))\Lambda^{(e)}$$
$$+ \psi'_n(k_2c)\zeta_n(k_2b) - \psi_n(k_2b)\zeta_n(k_2c) \Big] \tag{50}$$

$$\alpha_n^{(m)} = \left\{ \frac{\zeta_n(k_0c)}{\zeta'_n(k_0c)} + \frac{\Lambda^{(m)}}{\sqrt{\varepsilon_2}} \right\}^{-1} \Big[(\psi'_n(k_2c)\zeta'_n(k_2b) - d'_n)\Lambda^{(m)}$$
$$+ \psi'_n(k_2b)\zeta_n(k_2c) - \psi_n(k_2c)\zeta'_n(k_2b) \Big] \tag{51}$$

$$\Lambda^{(e)} = \frac{\psi'_n(k_2c)A_n^{(e)} + \zeta'_n(k_2c)B_n^{(e)}}{\psi_n(k_2c)A_n^{(e)} + \zeta_n(k_2c)B_n^{(e)}}, \tag{52}$$

$$\Lambda^{(m)} = \frac{\psi_n(k_2c)A_n^{(m)} + \zeta_n(k_2c)B_n^{(m)}}{\psi'_n(k_2c)A_n^{(m)} + \zeta'_n(k_2c)B_n^{(m)}} \tag{53}$$

$$A_n^{(e)} = \sqrt{\varepsilon_1/\varepsilon_2}\,\psi_n(k_1a)\zeta'_n(k_2a) - \psi'_n(k_1a)\zeta_n(k_2a), \tag{54}$$

$$B_n^{(e)} = \psi_n(k_2a)\psi'_n(k_1a) - \sqrt{\varepsilon_1/\varepsilon_2}\,\psi'_n(k_2a)\psi_n(k_1a) \tag{55}$$

$$A_n^{(m)} = \psi_n(k_1a)\zeta'_n(k_2a) - \sqrt{\varepsilon_1/\varepsilon_2}\,\psi'_n(k_1a)\zeta_n(k_2a), \tag{56}$$

$$B_n^{(m)} = \sqrt{\varepsilon_1/\varepsilon_2}\,\psi_n(k_2a)\psi'_n(k_1a) - \psi'_n(k_2a)\psi_n(k_1a) \tag{57}$$

Note that $\Delta_n^{(e,m)} \to 0$ if $n \to \infty$ or $k_0c \to 0$.

The DSEs (44) and (45) can be further transformed with the aid of the Abel integral transform (see [15]) for the Legendre associated functions and also the identities

$$\tan(\theta/2) = \frac{2\sqrt{2}}{\pi} \frac{1}{\sin\theta} \int_0^\theta \frac{\sin(\varphi/2)\sin\varphi}{\sqrt{\cos\varphi - \cos\theta}}d\varphi, \tag{58}$$

$$\cot(\theta/2) = \frac{2\sqrt{2}}{\pi} \frac{1}{\sin\theta} \int_\theta^\pi \frac{\cos(\varphi/2)\sin\varphi}{\sqrt{\cos\theta - \cos\varphi}}d\varphi \tag{59}$$

This procedure leads to a new DSE in terms of the trigonometric functions.

$$\begin{cases} \displaystyle\sum_{n=1}^\infty \left(1 - \Delta_n^{(e)}\right)\tilde{z}_n^{(e)} \sin\left(n+\frac{1}{2}\right)\theta = -2k_0cA\,\sin\frac{1}{2}\theta, \theta \in [0,\theta_0] \\[2mm] \displaystyle\sum_{n=1}^\infty \frac{\tilde{z}_n^{(e)} - \alpha_n^{(e)}}{2n+1}\cos\left(n+\frac{1}{2}\right)\theta = B\cos\frac{1}{2}\theta, \qquad \theta \in (\theta_0, \pi] \end{cases} \tag{60}$$

$$\begin{cases} \displaystyle\sum_{n=1}^\infty \frac{\left(1 - \Delta_n^{(m)}\right)\tilde{z}_n^{(m)}}{2n+1} \sin\left(n+\frac{1}{2}\right)\theta = -\frac{A}{k_0c}\sin\frac{1}{2}\theta, \ \ \theta \in [0,\theta_0] \\[2mm] \displaystyle\sum_{n=1}^\infty \left(\tilde{z}_n^{(m)} - \alpha_n^{(m)}\right)\cos\left(n+\frac{1}{2}\right)\theta = B\cos\frac{1}{2}\theta, \qquad \theta \in (\theta_0, \pi] \end{cases} \tag{61}$$

Now, after differentiation in θ of those equations that contain the factor $1/(2n+1)$ and application of the inverse Fourier transform, we obtain two coupled infinite-matrix equations,

$$\tilde{z}_m^{(e)} - \sum_{n=1}^\infty \tilde{z}_n^{(e)}\Delta_n^{(e)}R_{nm} = -(2k_0cA + B)R_{0m}$$
$$+ \sum_{n=1}^\infty \alpha_n^{(e)}\left(\delta_n^m - R_{nm}\right), \quad m = 1, 2, \dots \tag{62}$$

$$\tilde{z}_m^{(m)} - \sum_{n=1}^\infty \tilde{z}_n^{(m)}\Delta_n^{(m)}Q_{nm} = -\left[A(2k_0c)^{-1} + B\right]Q_{0m}$$
$$+ \sum_{n=1}^\infty \alpha_n^{(m)}\left(\delta_n^m - Q_{nm}\right), \quad m = 1, 2, \dots \tag{63}$$

$$2k_0cR_{00}A - (1 - R_{00})B = \sum_{n=1}^\infty \left[\tilde{z}_n^{(e)}\Delta_n^{(e)} - \alpha_n^{(e)}\right]R_{n0}, \tag{64}$$

$$(2k_0c)^{-1}Q_{00}A - (1 - Q_{00})B = \sum_{n=1}^\infty \left[\tilde{z}_n^{(m)}\Delta_n^{(m)} - \alpha_n^{(m)}\right]Q_{n0}, \tag{65}$$

where $Q_{nm}(\theta_0)$ are the same as (25) and

$$R_{nm}(\theta_0) = \frac{\sin(n-m)\theta_0}{\pi(n-m)} - \frac{\sin(n+m+1)\theta_0}{\pi(n+m+1)} \tag{66}$$

Finally, after exclusion of the constants A and B, the resulting coupled matrix equations are ($m = 1, 2, \dots$)

$$\tilde{z}_m^{(e)} + \sum_{n=1}^{\infty} \left[A_{nm}^{(e,e)} \tilde{z}_n^{(e)} + A_{nm}^{(e,m)} \tilde{z}_n^{(m)} \right] = B_m^{(e)},$$

$$\tilde{z}_m^{(m)} + \sum_{n=1}^{\infty} \left[A_{nm}^{(m,e)} \tilde{z}_n^{(e)} + A_{nm}^{(m,m)} \tilde{z}_n^{(m)} \right] = B_m^{(m)}, \tag{67}$$

where

$$A_{nm}^{(e,e)} = \Delta_n^{(e)} \left[R_{nm} - \frac{2R_{n0}}{W} R_{0m} Q_{00} - 2(k_0 c)^2 R_{0m}(1 - Q_{00}) \right], \tag{68}$$

$$A_{nm}^{(e,m)} = \Delta_n^{(m)} \frac{2k_0 c}{W} R_{0m} Q_{n0}, \quad A_{nm}^{(m,e)} = \Delta_n^{(e)} \frac{Q_{0m} R_{n0}}{2W k_0 c}, \tag{69}$$

$$A_{nm}^{(m,m)} = \Delta_n^{(m)} \left\{ -Q_{nm} + Q_{n0} \left[2k_0 c Q_{0m} R_{00} \right. \right.$$
$$\left. \left. - \frac{Q_{0m}}{2k_0 c} R_{0m}(1 - R_{00}) \right] \right\} \tag{70}$$

$$B_m^{(e)} = \alpha_n^e \left(\delta_n^m - R_{nm} \right) + 2R_{n0} \left[R_{0m} Q_{00} - 2(k_0 c)^2 R_{0m}(1 - Q_{00}) \right] \tag{71}$$

$$B_m^{(m)} = \alpha_n^e \left[\delta_n^m - R_{nm} + (W k_0 c)^{-1} Q_{0m} R_{n0} \right]$$
$$+ Q_{n0} \alpha_n^m \left[2k_0 c Q_{0m} R_{00} - (2k_0 c)^{-1} Q_{0m} R_{0m}(1 - R_{00}) \right] \tag{72}$$

$$W = -2k_0 c R_{00}(1 - Q_{00}) - (2k_0 c)^{-1} Q_{00}(1 - R_{00}) \tag{73}$$

Since $\sum_{m,n=0}^{\infty} |A_{nm}^{(s,t)}|^2 < \infty$, $s, t = e, m$, (67) is an operator Fredholm equation of the second kind in the space of numerical sequences $l_2^2 = l_2 \times l_2$ ($\tilde{z}^{(s)} \in l_2$ for $s = e, m$) under the condition that $\{B_m^{(s)}\}_{m=0}^{\infty} \in l_2$ for $s = e, m$, which holds true provided that $a < b < c$. This guarantees the convergence of the solutions of (67) with each of the four blocks truncated to a finite order N to the exact one by the l_2^2-norm.

In the TMD-excited antenna modelling, we are interested in the radiation conductance defined as

$$G = 2\bar{P}/|I_0^m|^2, \tag{74}$$

where the power radiated by the antenna is

$$\bar{P} = \left(\frac{q}{4\pi b} \right)^2 \frac{\pi}{Z_0} \sum_{n=1}^{\infty} (2n+1) \left(|z_n^{(e)}|^2 + |z_n^{(m)}|^2 \right) \tag{75}$$

This value is conveniently normalised by the radiation conductance associated with a dipole in the free space.

$$G_0 = (6\pi Z_0)^{-1} k_0^2 q^2 / |I_0^m|^2 \tag{76}$$

The directivity of the antenna is defined by (29), where correct account of the power radiated in the main-beam direction yields.

$$D = \frac{1}{8\pi Z_0 \bar{P}} \left(\frac{q}{b} \right)^2$$

$$\times \left| \sum_{n=1}^{\infty} (-i)^n \frac{(2n+1)}{n(n+1)} \left[iz_{(e)}^n \frac{P_1^n(\cos\theta)}{\sin\theta} + z_{(m)}^n \frac{dP_1^n(\cos\theta)}{d\theta} \right] \right|^2 \Bigg|_{\theta = \theta_{\max}} \tag{77}$$

Note that for the TMD in the free space the directivity is the same as for the RED, that is, $D_0 = 3/2$; however, $\theta_{\max} = 0$ and $180°$.

3 | CONVERGENCE AND ACCURACY OF THE ALGORITHM

The accuracy of the spherical functions' calculation can be easily kept at machine precision. Therefore, the resulting computational error of our algorithm is determined solely by the matrix truncation error. The rate of convergence of the algorithm can be estimated by plotting the normalised computational error, $e(N)$, in the sense of the l_2^2 norm versus the matrix truncation number N. The results of such a test are presented in Figure 2.

As one can see, the error decreases rapidly enough to provide a several-digit accuracy for the lenses of moderately large size using small N. For comparison, if one uses an FDTD algorithm, the number of equations needed for solving the considered problem with a reasonable accuracy would exceed many hundred thousands

Our analysis shows that the matrix truncation number needed to obtain the required numerical accuracy is a function of the lens parameters, namely its electrical size and the relative thickness of the shell, and does not depend on the angular width of the reflector. As we have found, a simple empirical formula for the truncation number can be derived. For example, for the relative accuracy of 10^{-4} in the numerical solution of the RED-case equations, the matrix truncation order should be $N \geq \max\{k_0 c \sqrt{\varepsilon_2}, k_0 a \sqrt{\varepsilon_1}\} + c/h + 10$. In the case of the TMD excitation, we have a block-type 2×2 matrix. Then the same rule must be applied to the truncation of each of the four blocks of this matrix. Therefore, when computing the dependences of the lens field's characteristics on the frequency or other parameters, except the angular size of the reflector θ_0, one has to adapt the truncation number in line with the mentioned rule.
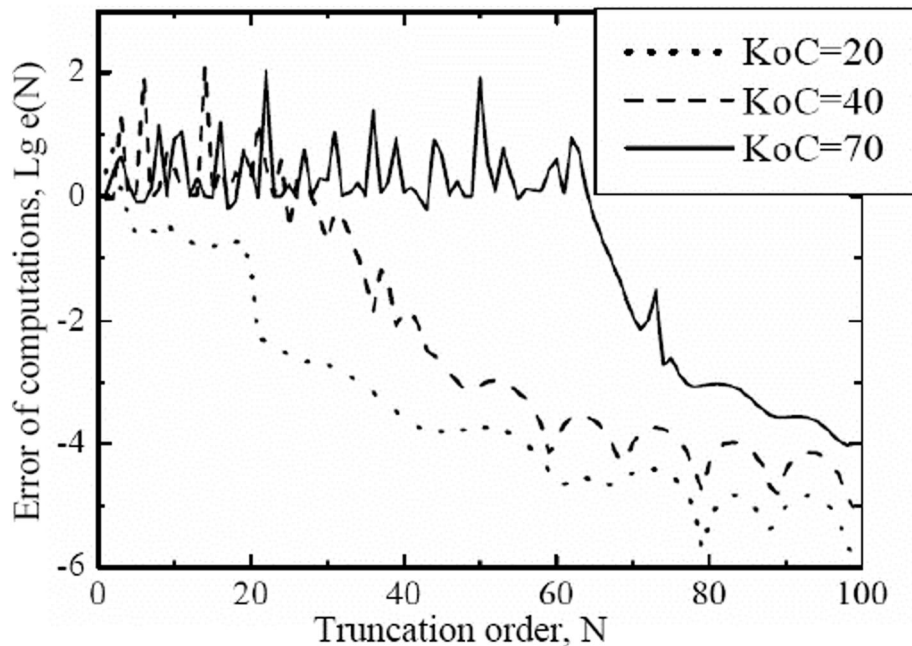
FIGURE 2 Normalised computational error versus the matrix size for $a/c = 0.9$, $\theta_0 = 18°$ and $\varepsilon_2 = 1.3$, $\varepsilon_1 = 1$ for three values of the normalised frequency in the case of radial Hertz electric dipole excitation

4 | PERFORMANCE OF DOUBLE-LAYER QUASI-LUNEBURG LENS FED BY ON-AXIS RED WITH REFLECTOR

The classical spherical Luneburg lens has its relative dielectric permittivity varying as $\varepsilon(r) = 2 - (r/c)^2$, where c is the lens radius [2]. Discrete Luneburg lenses approximate this dependence in a step-like manner [5], using a finite number of spherical shells each having a constant value of permittivity. The larger the number of shells and the lens radius, the closer the lens' behaviour to the GO prediction.

However, in practice it is very difficult and expensive to manufacture a lens with large number of shells. Therefore, there is significant interest in the simple double-shell lenses [8]. We will concentrate our numerical simulations on the case of a 'quasi-Luneburg' double-layer ILA, that is, the lens with the inner core having dielectric constant $\varepsilon_1 = 2$ and the outer shell with $\varepsilon_2 = 1.1$. The elementary dipole location will be the same in all the examples, $b/c = 0.95$.

The results are presented in Figures 3–6. As one can see, the best directivity is achieved for the core-shell aspect value $a/c = 0.9$. For such a lens, the radiated power oscillates with the frequency, while the directivity grows within a linear envelope and the main-beam angle is close to 180°.

The most striking feature of these plots is the presence of very intensive and periodic in-frequency resonances if the frequency gets larger than some value determined by the radius and the dielectric constant of the higher-permittivity core. In these resonances, the radiation resistance jumps up; however, the directivity drops to significantly lower values than the resonances, and the main beam deviates

further from 180°. This is because the resonances are associated with the whispering-gallery modes (WGM), whose fields vary as $\cos m\theta$, thus radiating into $2m$ equally intensive beams. Each time when a WGM is excited, its $2m$ identical beams flash up in the radiation pattern, spoiling the collimation effect of the lens that has the GO, that is, the broadband and nature.

The examples of the far-field radiation patterns are shown in Figure 6. They are the cross-sections of the rotationally symmetric 'hollow-cone' patterns because an on-axis RED does not excite the field along the axis of symmetry. One can see that the shape and direction of the main beam depend on the score-shell aspect value. The shape and level of the side-lobes are even more sensitive to this parameter—the smaller the aspect, the better.

Consider now the frequency dependences of the same antenna characteristics as before for the different values of the PEC reflector size, θ_0. One can see that the presence of the reflector leads to enhancement of the resonances (Figure 7).

Even more interesting is the observation that a small reflector is able to improve the directivity of the small-size quasi-Luneburg lens (see Figure 8).

For example, this improvement can be at 2 times if $k_0 c = 15$, $a/c = 0.9$ and $\theta_0 = 36^0$, if we consider the envelope of each dependence. Still, the WGM resonances spoil the directivity if the lens size is larger than $k_0 c \approx 12$.

4.1 | Effect of dielectric losses

In reality, there are no lossless dielectrics and, moreover, no ideally smooth spherical shells. Instead, the surface roughness
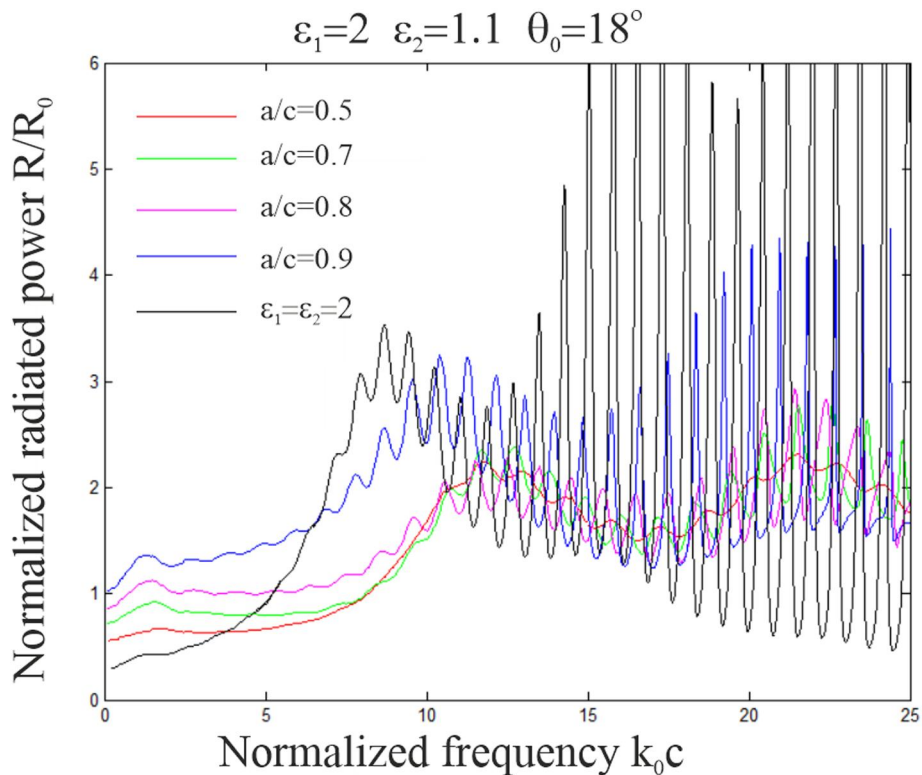
FIGURE 3 Normalised power radiated by the on-axis radial Hertz electric dipole versus the normalised frequency, for several core/shell aspect values in the quasi-Luneburg lens with a $\theta_0 = 18^0$ reflector
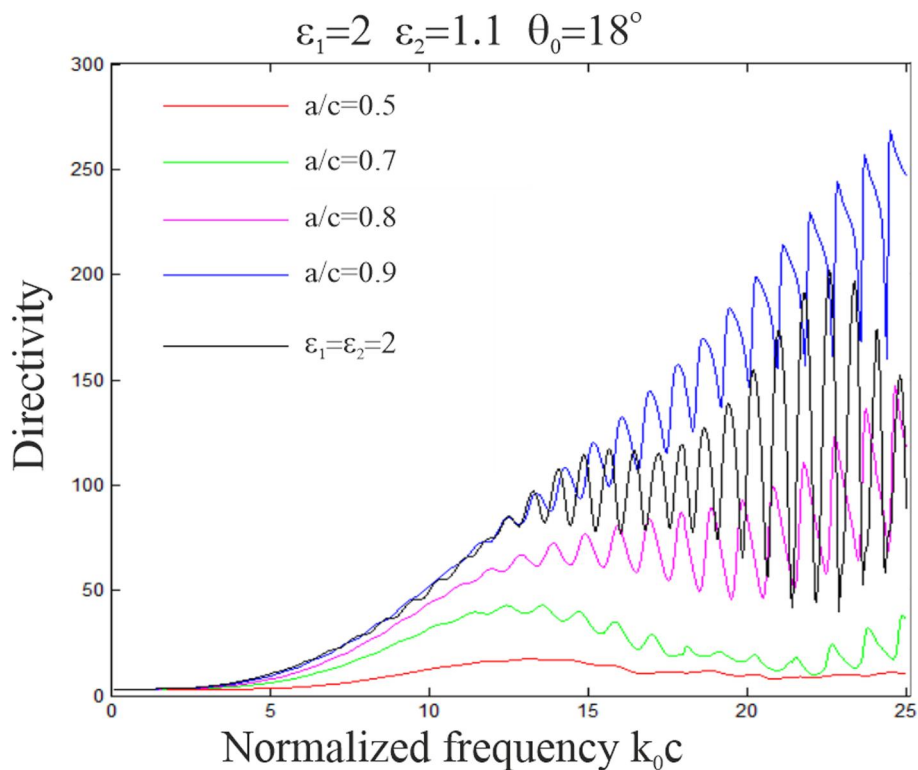

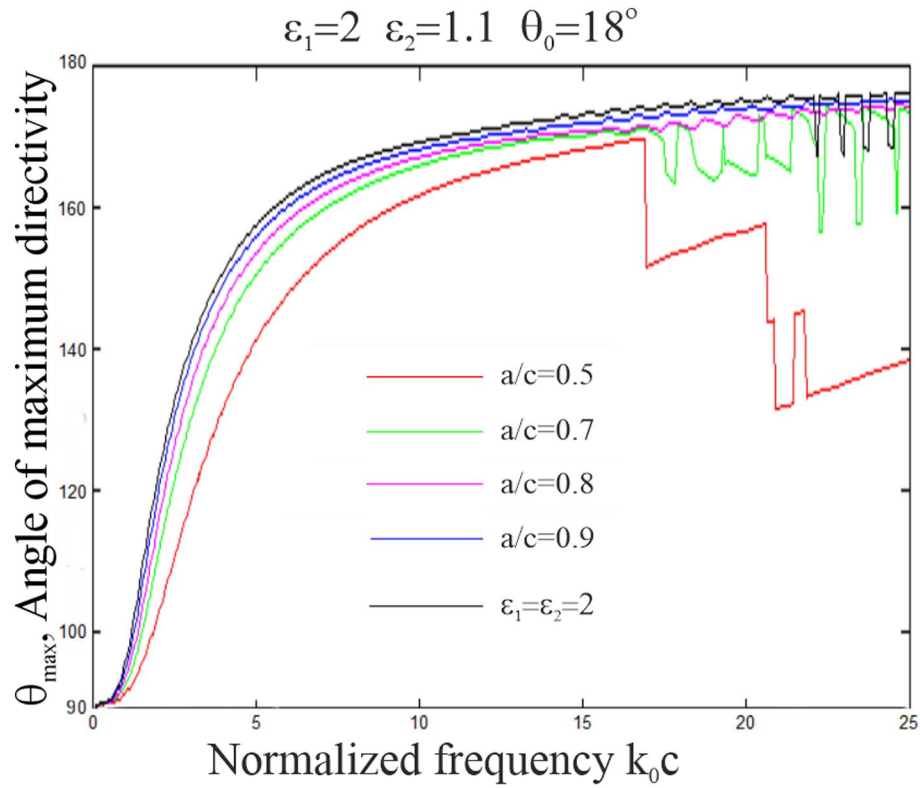**FIGURE 4** The same as in Figure 3, but for the directivity

FIGURE 5 The same as in Figures 3 and 4, but for the main beam direction
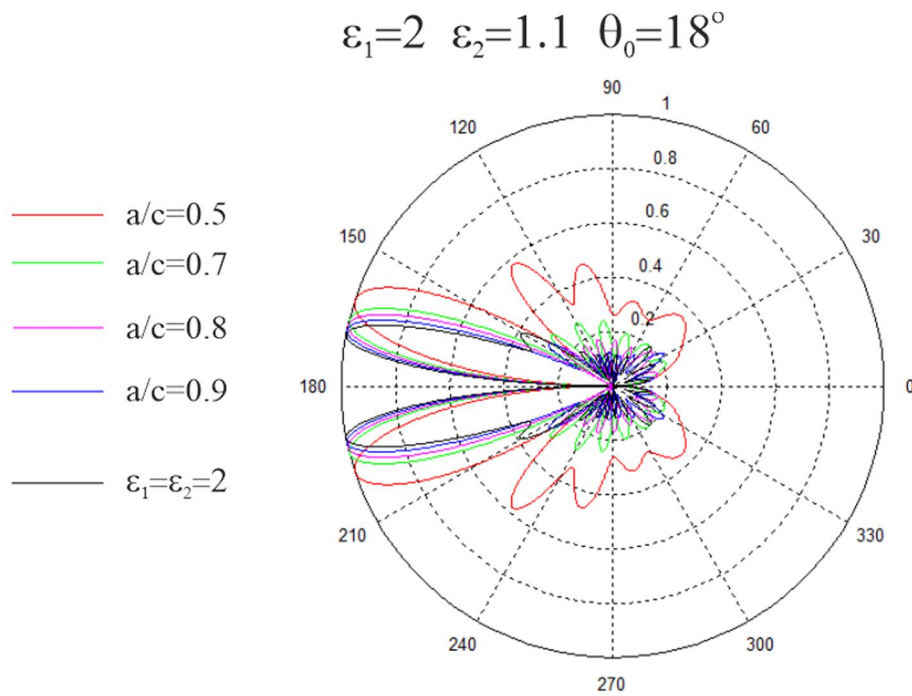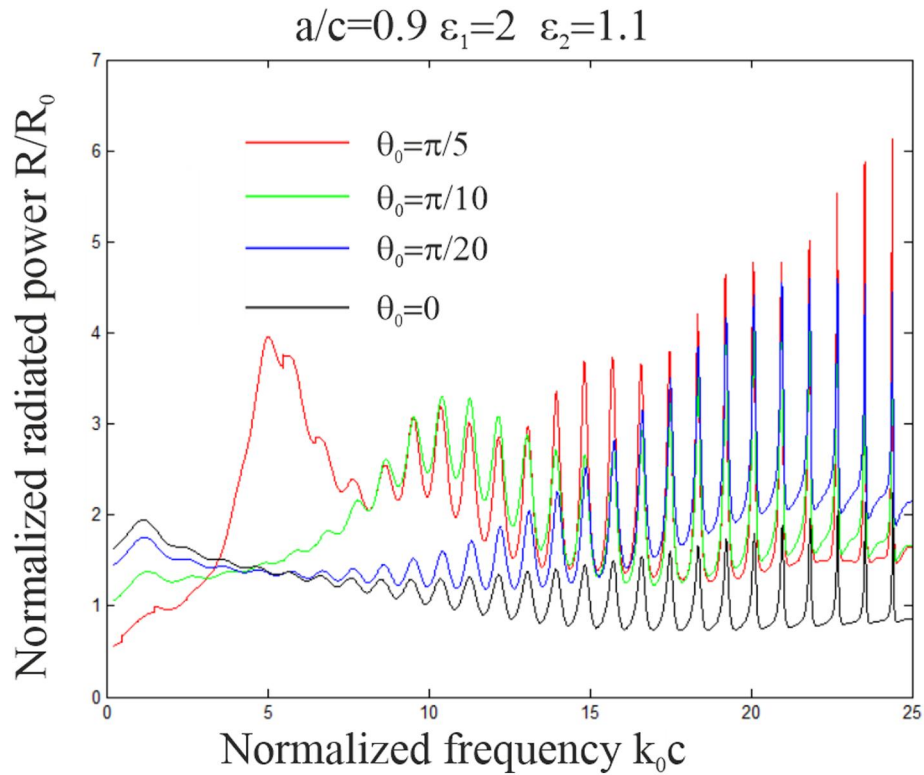

FIGURE 6 Normalised far-field radiation patterns for on-axis radial Hertz electric dipole feeding the quasi-Luneburg lens with several values of the core/shell aspect values and $\theta_0 = 18^0$ reflector

FIGURE 7 Normalised power radiated by on-axis radial Hertz electric dipole versus the normalised frequency, for several values of the reflector angular width θ_0 and core/shell aspect value $a/c = 0.9$
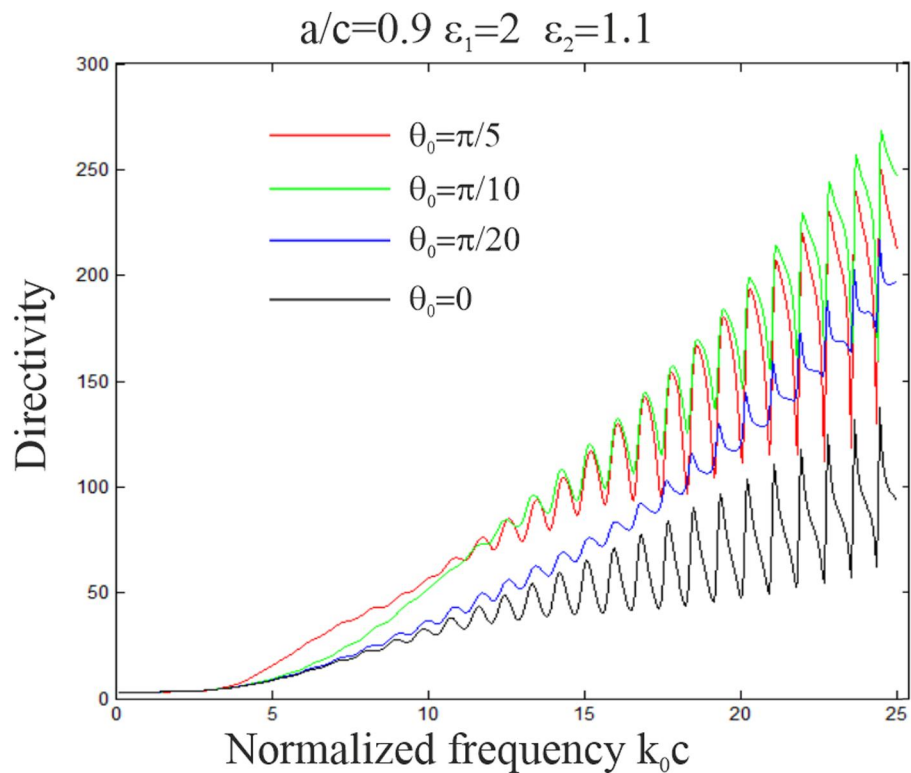
FIGURE 8 The same as in Figure 9, but for the directivity
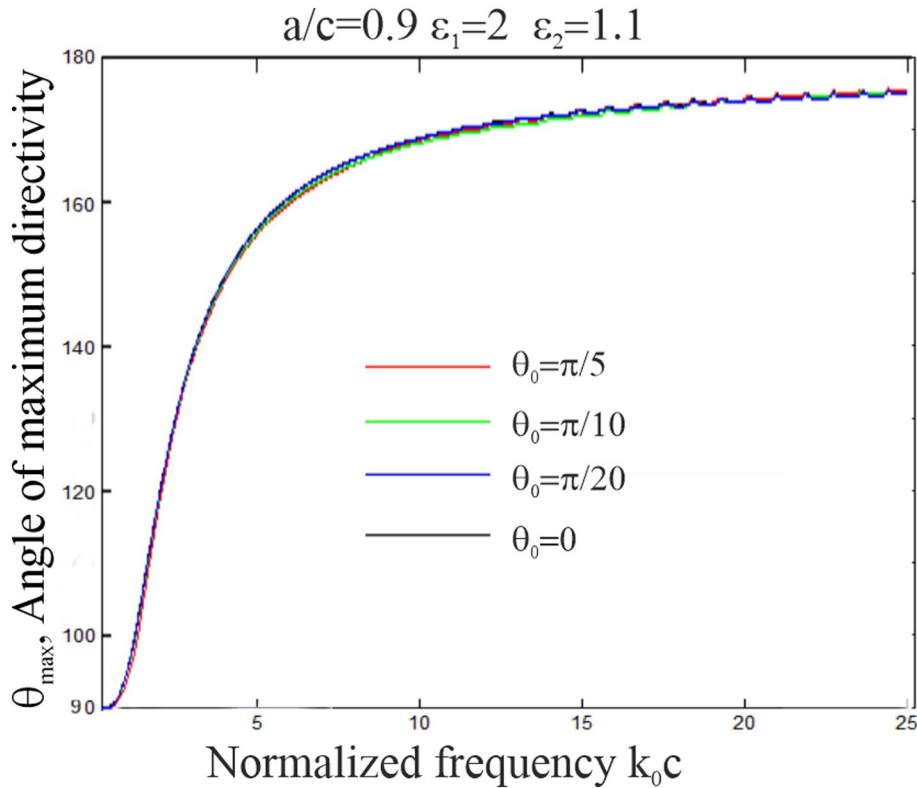
FIGURE 9 The same as in Figure 8, for the main beam direction

and internal dielectric losses are always present and damp the resonances.

Figure 10–15 give information on how much the performance of the quasi-Luneburg lens depends on the shell losses. The WGM resonances are especially sensitive to the losses in the shell because these modes have the fields concentrated near the core's outer surface.

It is seen that, indeed, the effect of smoothing the WGM resonances takes place. However, the value of the losses should be optimally selected in order to avoid overall reduction of directivity–this feature happens to be provided if the losses are $\mathrm{Im}\,\varepsilon_2 \approx 0.1$. Smaller losses do not suppress very sharp WGM resonances while greater losses lead to unwanted reduction of the lens antenna directivity.

In our analysis, we do not study the effect of the surface roughness. However, introduction of the dielectric losses in the thin low-refractive-index shell of a lens antenna is very similar to the roughening of the shell surface.

This analogy follows, for instance, from the analysis of the effect of a periodic corrugation on the modes of the circular dielectric resonators, published in [22]. As soon as the period or depth of corrugations becomes close to the WGM wavelength, its Q-factor gets spoiled dramatically.

5 | NUMERICAL RESULTS FOR DOUBLE-LAYER DIELECTRIC LENS FED BY ON-AXIS TMD WITH REFLECTOR

Unlike the RED, the on-axis TMD enables one to obtain the main beam of the considered ILA looking in the forward direction, that is, at $\theta = 180^0$. The results of computations are presented in Figure 16–20, for several values of the core-shell aspect ratio and reflector angular width; the dipole location is fixed as $b/c = 0.95$.

The frequency scan of the normalised radiation power is presented in Figure 16. It shows an interplay of the resonance phenomena and the GO beam collimation similar to the case of the RED-fed ILA. In particular, the WGM resonances become the dominating feature as the frequency is increased.

The frequency scans of the directivities in two main planes of the antenna are shown in Figures 17 and 18. Comparison of them with similar plots of directivity of a RED-fed quasi-Luneburg lens (see Figure 4) shows much larger values. This is because the TMD source has a non-zero primary field along the antenna axis, which is in better agreement with the GO collimation effect. The directivity, however, is destroyed each time when the frequency of operation hits a WGM resonance.
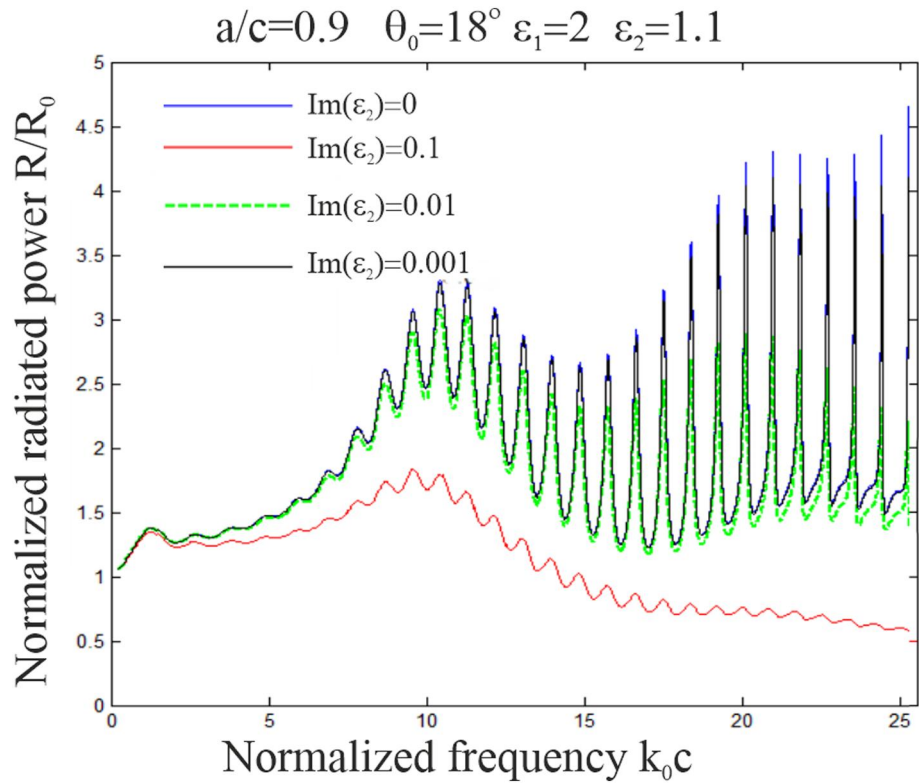
FIGURE 10 Normalised power radiated by on-axis radial Hertz electric dipole versus normalised frequency for the quasi-Luneburg lens with the core-shell aspect 0.9 and a $\theta_0 = 18^0$ reflector, with and without the losses in the shell
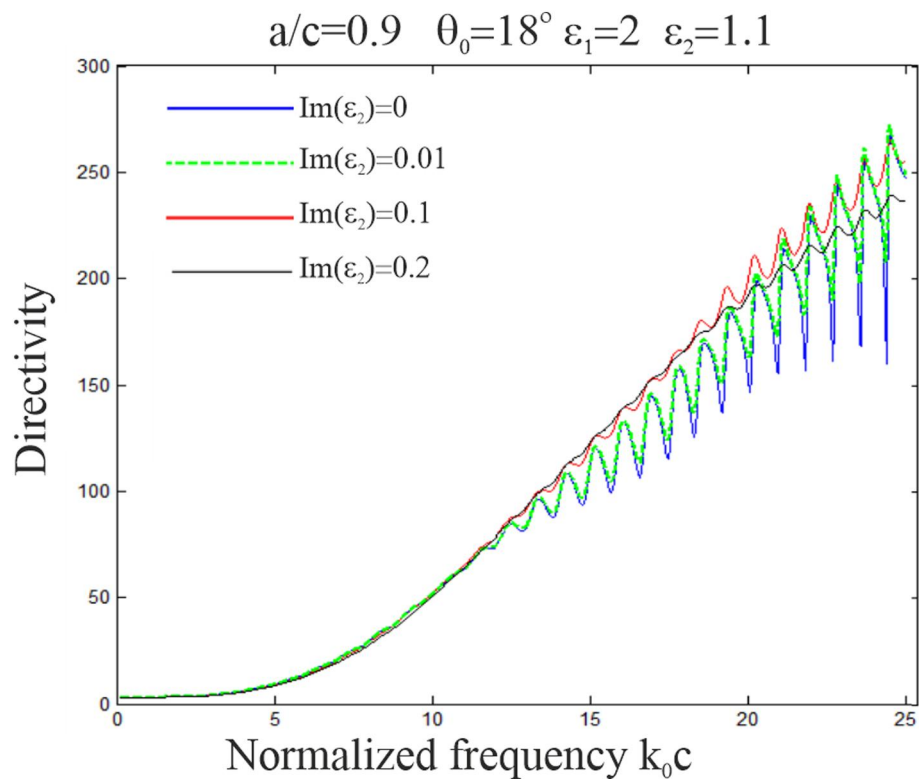

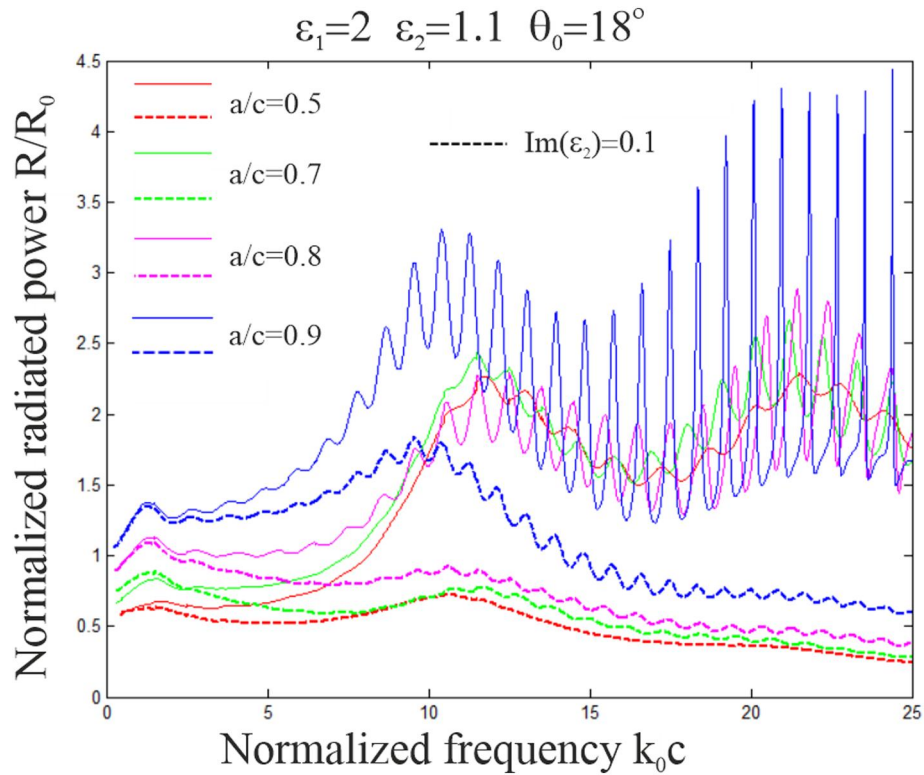**FIGURE 11** The same as in Figure 9, but for the directivity

FIGURE 12 Normalised power radiated by on-axis radial Hertz electric dipole versus normalised frequency, for several core/shell aspect values in the quasi-Luneburg lens with and w/o optimal losses
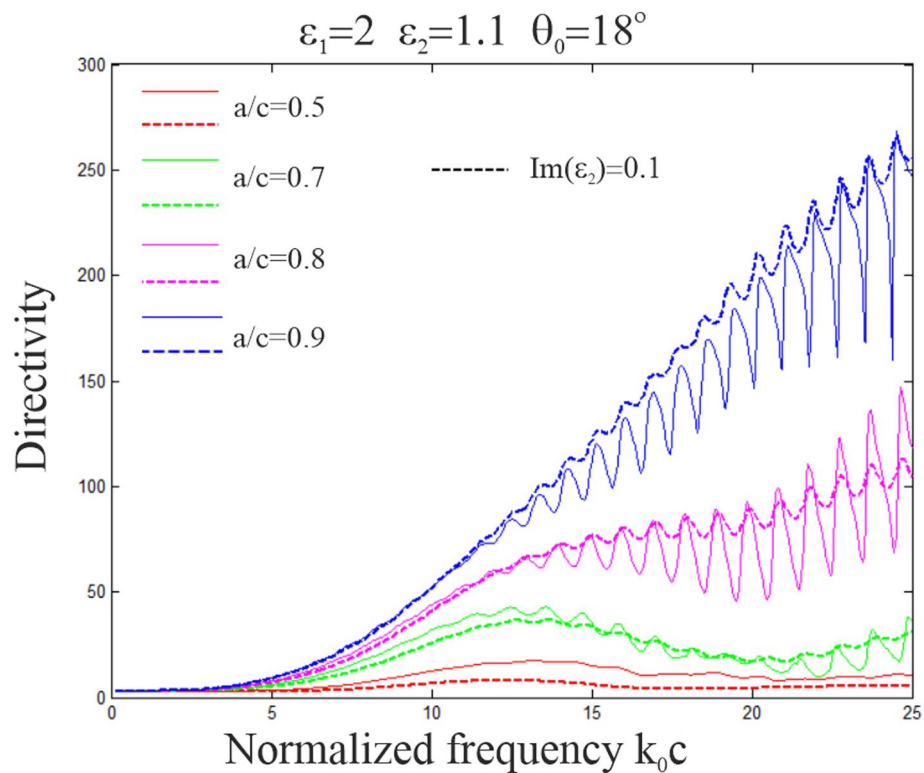

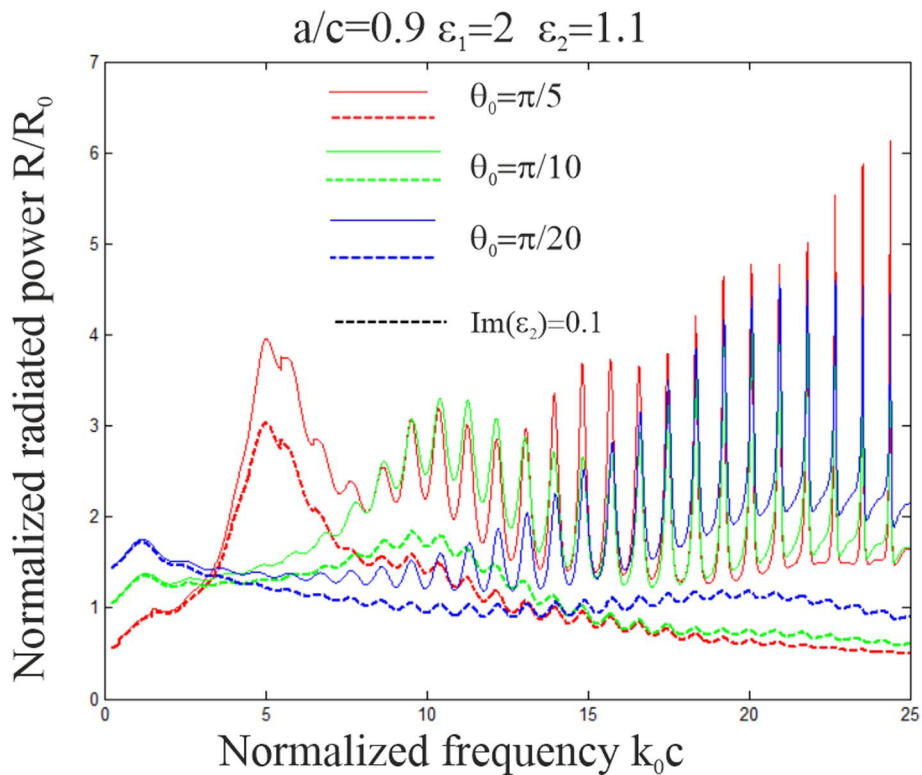**FIGURE 13** The same as in Figure 12, however, for the directivity

FIGURE 14 Normalised power radiated by on-axis radial Hertz electric dipole versus normalised frequency, for several reflector size values in the quasi-Luneburg lens with and w/o optimal shell losses
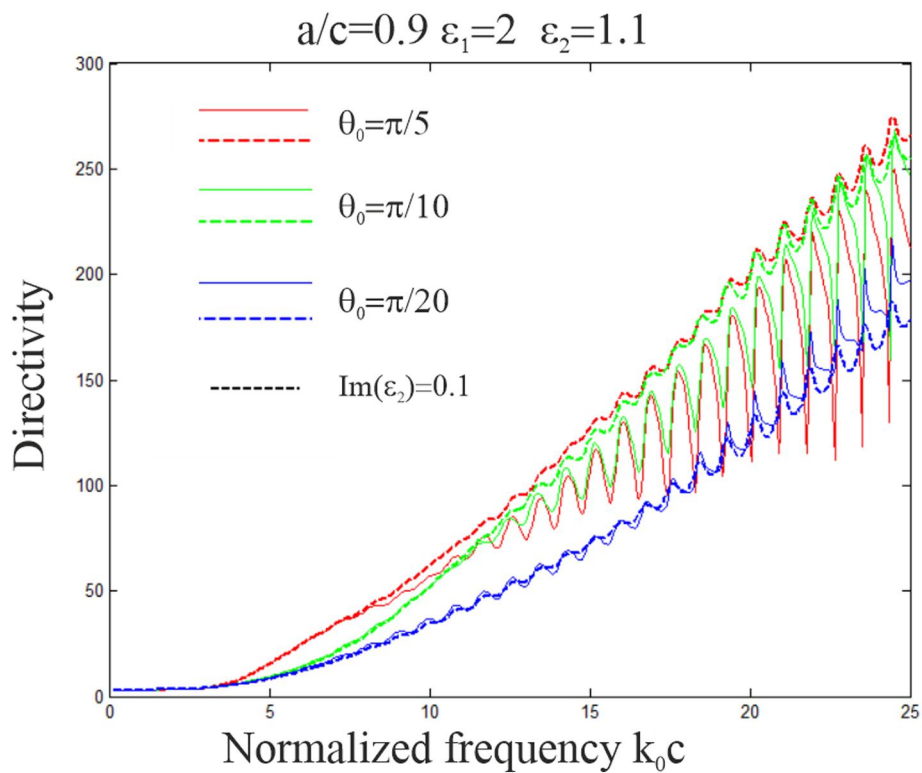

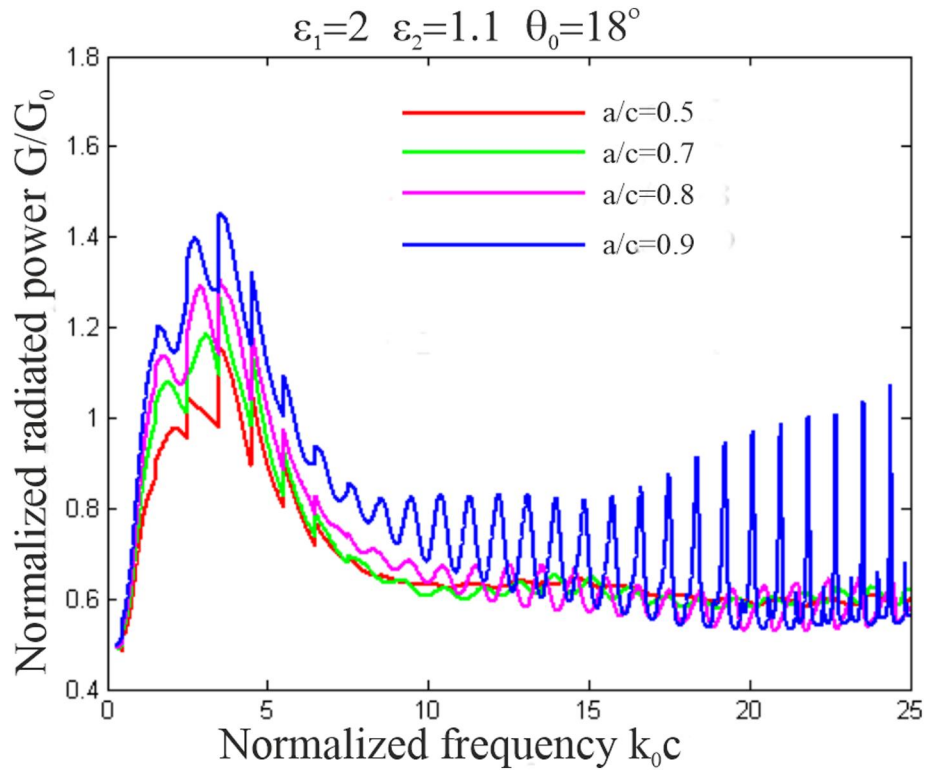**FIGURE 15** The same as in Figure 14, but for the directivity

FIGURE 16 Normalised power radiated by on-axis TMD versus the normalised frequency, for several core/shell aspect values in the quasi-Luneburg lens with a $\theta_0 = 18^0$ reflector
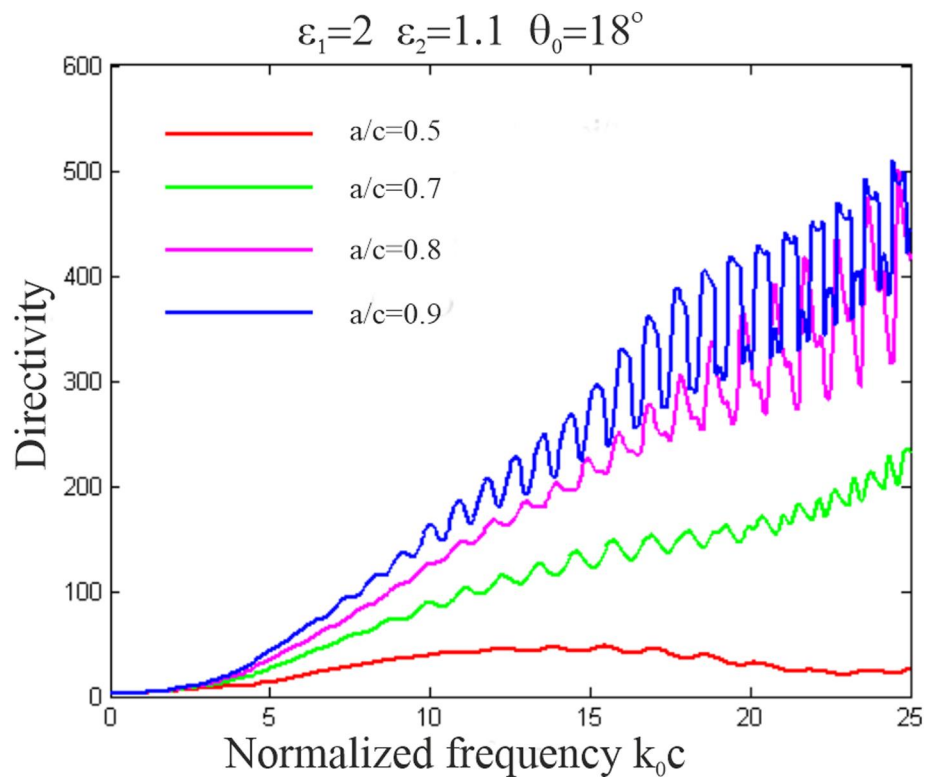

FIGURE 17 Directivity in the E-plane, $\varphi = 90^0$, versus the normalised frequency for the same quasi-Luneburg lens configurations as in Figure 16

$$\varepsilon_1=2 \quad \varepsilon_2=1.1 \quad \theta_0=18°$$

FIGURE 18 The same as in Figure 17, but in the H-plane

$$a/c=0.9 \quad \varepsilon_1=2 \quad \varepsilon_2=1.1$$

FIGURE 19 Normalised radiated power of the on-axis tangential Hertz magnetic dipole fed quasi-Luneburg lens versus the normalised frequency, for several reflector sizes and core-shell aspect $a/c = 0.9$

FIGURE 20 Directivity in the H-plane, $\varphi = 0$, versus normalised frequency for the same quasi-Luneburg lens configurations as in Figure 19

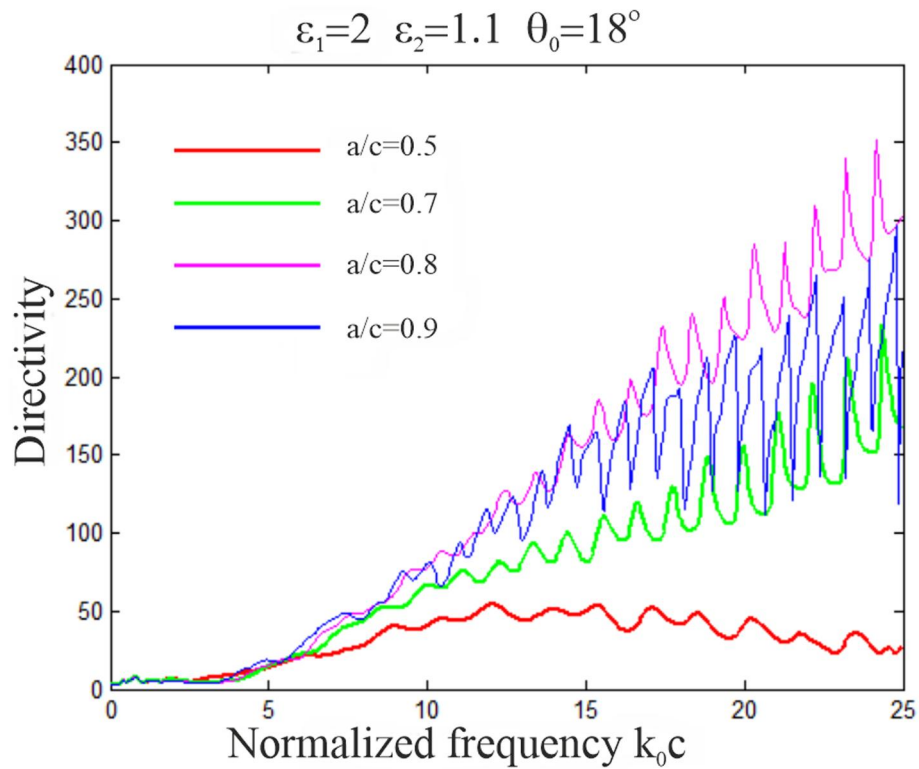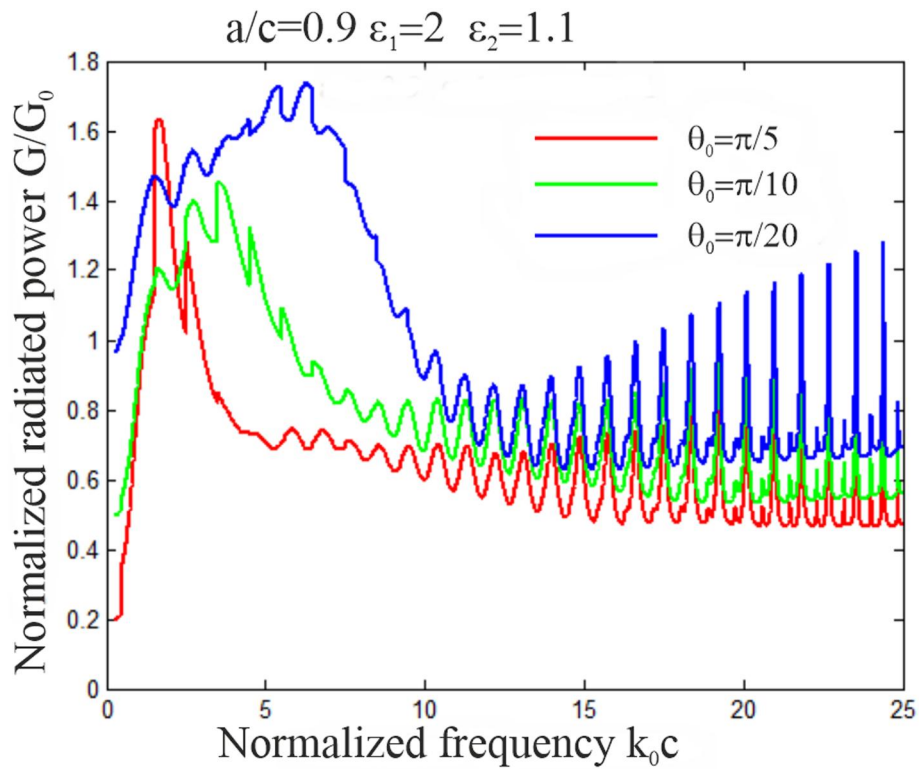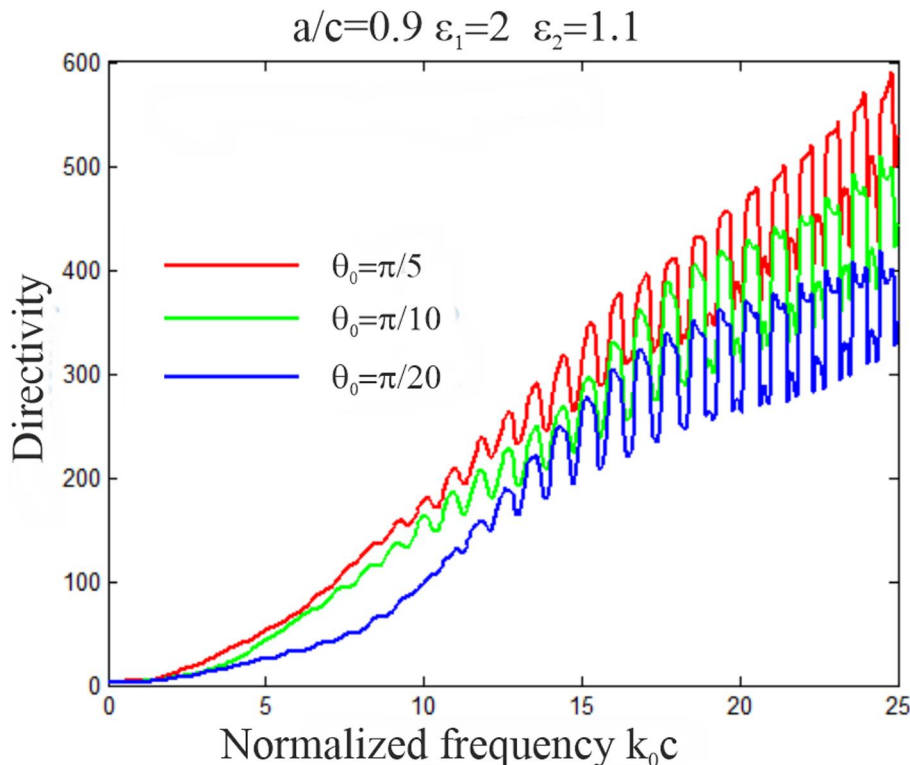In Figures 19 and 20, we present similar plots; however, they are computed for several different values of the reflector size, θ_0.

This is because in the resonance, a flash of the WGM eigenfield that has many identical beams occurs in the far-field pattern. One may anticipate that the ripples in directivity can be smoothed by the introduction of the losses in the shell of the quasi-Luneburg lens, similar to the RED excitation case.

One may conclude that the small-reflector configurations show better directivity although they radiate with somewhat smaller input resistance.

In Figure 21, we show the normalised far-field angular radiation patterns of the studied lens antenna of several electric sizes. They are combined in pairs so that the left and the right-hand parts correspond to one half of the H-plane and the E-plane pattern, respectively. One can see the effect of the lens in the collimation of the main beam in the forward direction if the electrical size of the double-shell quasi-Luneburg lens gets larger.

6 | CONCLUSION

The basic equations have been derived and the numerical code has been developed for reliable and efficient full-wave numerical analysis of spherical double-layer lenses integrated with a conformal printed disk reflector, backing an RED or TMD source on the axis of rotation. The method follows [15–19]; it is based on the analytical regularisation of certain DSEs and reduces the scattering problem to a Fredholm second-kind matrix equation. Note that it is the static limit of the PEC spherical disk on a homogeneous sphere that is inverted analytically. After casting each of the problems to the Fredholm equations, a numerical solution of a few dozen lambda-size lenses takes just seconds on a moderate computer, and the accuracy is controlled and can be refined as necessary.

Using this efficient and accurate computational instrument, we have studied the performance of the quasi-Luneburg ILA where the massive core and the thin shell have dielectric constants 2 and 1.1, respectively. The primary source has been considered as either an RED or a TMD located on the lens axis and backed with a PEC spherical reflector conformal to the outer surface of the lens shell. Such ILAs appear to be promising as candidates for the use in the millimetre-wave frond-end applications, although they can suffer from sharp WGM resonances. To smooth these resonances without significant loss in directivity, one can introduce the losses in the shell layer. In view of the results, published in [22], it can be expected that the same smoothening effect can be provided by the roughening of the shell's inner or outer surface.

(a)

$\phi=0°$ $\phi=90°$

$k_0c=1.61$, $a/c=0.9$, $\theta_0=\pi/10$, $\varepsilon_1=2$, $\varepsilon_2=1.1$

(b)

$\phi=0°$ $\phi=90°$

$k_0c=2.08$, $a/c=0.9$, $\theta_0=\pi/10$, $\varepsilon_1=2$, $\varepsilon_2=1.1$

(c)

$\phi=0°$ $\phi=90°$

$k_0c=2.73$, $a/c=0.9$, $\theta_0=\pi/10$, $\varepsilon_1=2$, $\varepsilon_2=1.1$

(d)

$\phi=0°$ $\phi=90°$

$k_0c=3.49$, $a/c=0.9$, $\theta_0=\pi/10$, $\varepsilon_1=2$, $\varepsilon_2=1.1$

(e)

$\phi=0°$ $\phi=90°$

$k_0c=3.53$, $a/c=0.9$, $\theta_0=\pi/10$, $\varepsilon_1=2$, $\varepsilon_2=1.1$

(f)

$\phi=0°$ $\phi=90°$

$k_0c=9.46$, $a/c=0.9$, $\theta_0=\pi/10$, $\varepsilon_1=2$, $\varepsilon_2=1.1$
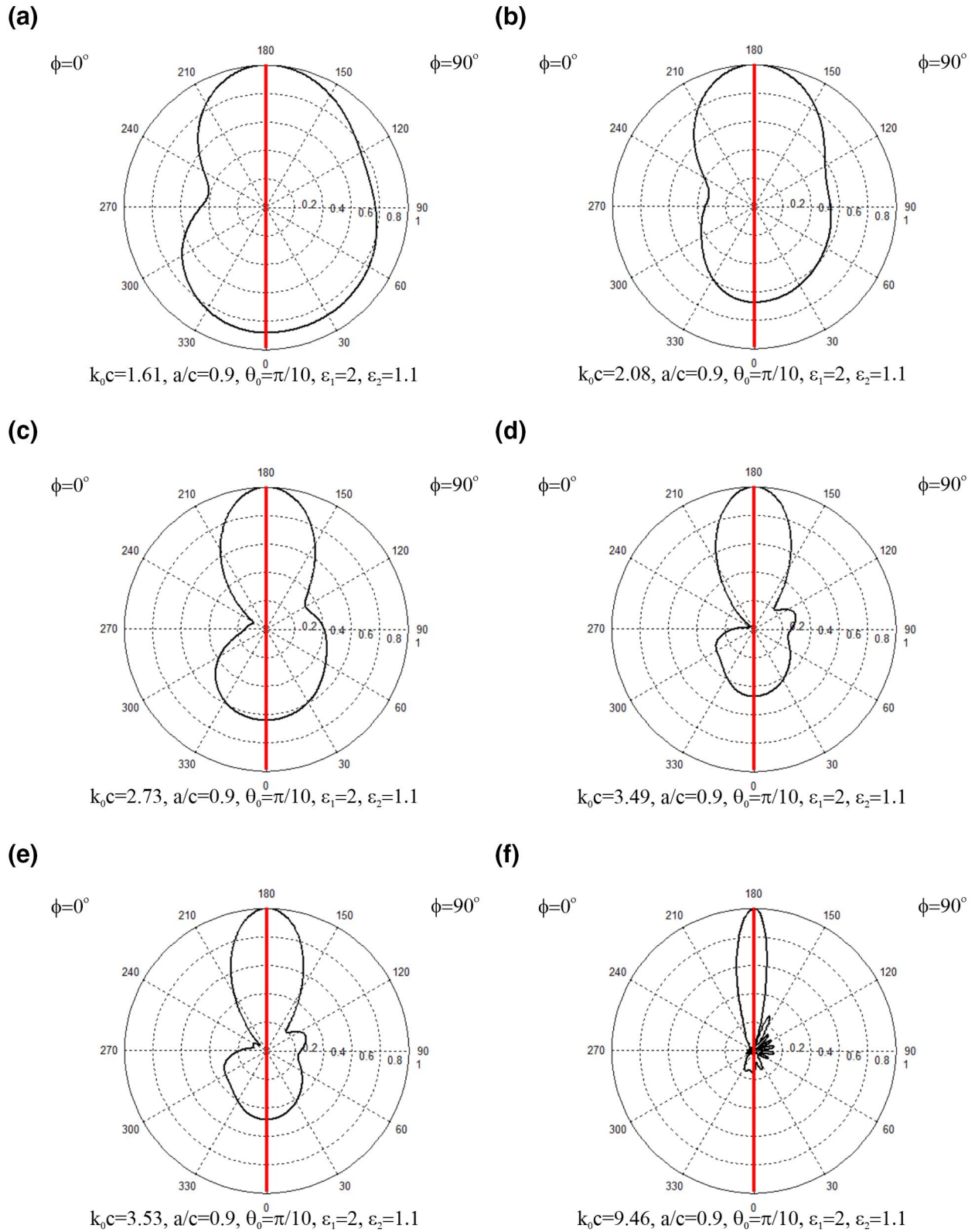

FIGURE 21 Normalized far-field radiation patterns for the on-axis tangential Hertz magnetic dipole feeding the quasi-Luneburg lens with the core-shell aspect value $a/c = 0.9$ and the $\theta_0 = 18^0$ reflector. The left (right) hand side of each pattern is for the H-plane (E-plane) section

ORCID

Sergii V. Dukhopelnykov [ID] https://orcid.org/0000-0002-0639-988X
Alexander I. Nosich [ID] https://orcid.org/0000-0002-3446-8168

REFERENCES

1. Bekefi, G., Farnell, G.W.: A homogeneous dielectric sphere as a microwave lens. Can. J. Physics. 34, 790–803 (1956)
2. Luneburg, R.K.: The mathematical theory of optics. Brown University Press. (2–nd ed. Berkeley Univ. California Press) (1944)
3. Gutman, A.S.: Modified Luneburg lens. J. Appl. Phys. 25, 855–859 (1954)
4. Tai, C.T.: The electromagnetic theory of the spherical Luneburg lens. Appl. Sci. Res. B7, 113–130 (1958)
5. Buckley, E.F.: Stepped-index Luneburg lenses. Electron. Design. (4), 86–89 (1960)
6. Rudduck, R.G., Walter, C.H.: A general analysis of geodesic Luneburg lens. IEEE Trans. Antennas Propag. 10(4), 444–449 (1962)
7. Gunderson, L.C., Holes, G.T.: Microwave Luneburg lens. Appl. Opt. 7(5), 801–804 (1968)
8. Mosallaei, H., Rahmat-Samii, Y.: Nonuniform Luneburg and two-shell lens antennas: radiation characteristics and design optimization. IEEE Trans. Antennas Propag. 49(1), 60–69 (2001)
9. Parfitt, A., et al.: A case for the Luneburg lens as the antenna elements for the square-kilometre array radio telescope. Radio Sci. Bulletin. 293, 32–37 (2000)
10. Schoenlinner, B., et al.: Wide-scan spherical-lens antennas for automotive radars. IEEE Trans. Microwave Theory Techn. 50(9), 2166–2175 (2002)
11. Boriskin, A.V., Nosich, A.I.: Whispering-gallery and Luneburg lens effects in a beam-fed circularly-layered dielectric cylinder. IEEE Trans. Antennas Propag. 50(9), 1245–1249 (2002)
12. Fuchs, B., et al.: Design optimization of multi-shell Luneburg lenses. IEEE Trans. Antennas Propag. 55(2), 283–289 (2007)
13. Nosich, A.I.: Method of analytical regularisation in wave-scattering and eigenvalue problems: foundations and review of solutions. IEEE Antennas Propag. Mag. 42, 34–49 (1999)
14. Bulygin, V.S., Nosich, A.I., Gandel, Y.V.: Nystrom-type method in three-dimensional electromagnetic diffraction by a finite PEC rotationally symmetric surface. IEEE Trans. Antennas Propag. 60(11), 4710–4718 (2012)
15. Vinogradov, S.S.: On the reflectivity of a spherical shield. Radiophys. Quant. Electron. 26(1), 78–88 (1983)
16. Ziolkowski, R.W., Johnson, W.A.: Electromagnetic scattering of an arbitrary plane wave from a spherical shell with a circular aperture. J. Mathem. Phys. 28(6), 1293–1314 (1987)
17. Radchenko, V.V., et al.: A conformal spherical-circular microstrip antenna: axisymmetric excitation by an electric dipole. Microwave Opt. Technol. Lett. 26(3), 176–182 (2000)
18. Rondineau, S., et al.: MAR-based analysis of a spherical-circular printed antenna with a finite ground excited by an axially-symmetric probe. IEEE Trans. Antennas Propag. 52, 1270–1280 (2004)
19. Rondineau, S., Nosich, A.I.: Printed-cavity and whispering-gallery-mode resonances in discrete Luneburg lens antenna integrated with a small double-disk feed. Proc. European Conf. Antennas Propag. (EuCAP-2006), European Space Agency Press. art. no 626 SP (2006)
20. Nikolic, N., Kot, J.S., Vinogradov, S.: Scattering by a Luneburg lens partially covered by a metallic cap. J. Electromagn. Waves Applic. 21(4), 549–563 (2007)
21. Vinogradov, S.S., et al.: Radar cross-section studies of spherical lens reflectors. Progress in Electromagn. Res. 72, 325–337 (2007)
22. Boriskina, S.V., et al.: Spectral shift and Q-change of circular and square-shaped optical microcavity modes due to periodic sidewall surface roughness. J. Opt. Soc. Am. B. 21(10), 1792–1796 (2004)